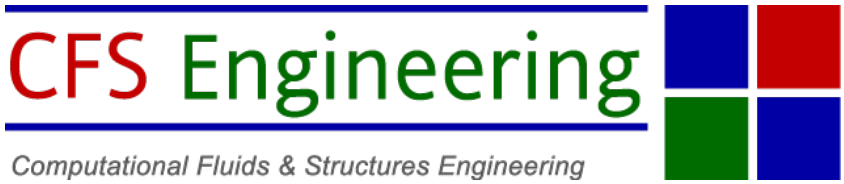

INTERNSHIP REPORT

June 9th 2025 – September 26th 2025

A Study of Thermo-Chemical Non-Equilibrium in Hypersonic Re-entry Vehicles Using Computational Fluid Dynamics

APPLIED TO THE RAM-C II TEST CASE

September 25, 2025

Author:

Justine Brun

Supervised by:

Jan Vos

Contents

Abstract 1

List of Figures 1

List of Tables 2

1 Introduction 3

2 RAM-C flight experiments 3

3 Simulation configuration 4
- 3.1 Geometry & meshing . . . 4
- 3.2 The NSMB solver . . . 5
- 3.3 Numerical parameters . . . 5
- 3.4 Flow model . . . 6
- 3.5 Kinetic model . . . 6
  - 3.5.1 Chemical species . . . 7
  - 3.5.2 Chemical reactions . . . 7
  - 3.5.3 Mass fractions . . . 8
- 3.6 Thermo-chemical models . . . 8
- 3.7 Boundary conditions . . . 8

4 Numerical simulation results 9
- 4.1 Conditions for RAM-C II test cases . . . 9
- 4.2 Electron number density distribution along the capsule skin . . . 9
- 4.3 Wall temperature . . . 11
  - 4.3.1 Distribution along the capsule skin . . . 12
  - 4.3.2 Distribution along the stagnation streamline . . . 13
- 4.4 Mass fractions along the stagnation streamline . . . 13
- 4.5 Temperatures along the stagnation streamline . . . 14
- 4.6 Multi-temperature model sensitivity analysis . . . 16
  - 4.6.1 Electronic non-equilibrium . . . 16
  - 4.6.2 Viscosity model influence . . . 17
  - 4.6.3 Influence of non-equilibrium chemistry and vibrational relaxation time . . . 19

5 Conclusions 21

Appendix A: Mass fraction distributions at 71 km 23

Abstract

This report gives an overview of the numerical study of thermo-chemical non-equilibrium phenomena in hypersonic re-entry flows, with a focus on the RAM-C II flight experiment conducted by NASA. The objective is to model and analyze key physico-chemical processes occurring in the shock layer around a re-entry vehicle, particularly those affecting electron number density, which directly influence communication blackout during atmospheric re-entry.

Simulations were carried out using the Navier–Stokes Multi Block (NSMB) solver, which was configured with detailed models, including thermo-chemical non-equilibrium effects. The study employs both 7-species and 11-species air models, as well as various kinetic and boundary condition configurations. Particular attention is given to the impact of wall temperature and species reactions on flow behavior.

Two RAM-C II flight conditions, at altitudes of 61 km and 71 km, were reproduced numerically. The simulation results include electron number density distributions along the capsule surface and stagnation line, as well as mass fraction and temperature profiles of key atmospheric species. These results were compared to available flight data to assess model accuracy. Thermo-chemical non-equilibrium models generally provided a better match with experimental data than chemical non-equilibrium models alone, although none perfectly reproduced the measurements.

This work emphasizes the challenges of accurately simulating high-altitude, high-speed flows, and underlines the ongoing need for improved modeling techniques and experimental validation.

List of Figures

1 Schematic of RAM-C II with probe and antenna locations from [1] 4
2 Modeling of the RAM-C geometry 4
3 Overview of the mesh used 4
4 Shock adaptation of the mesh 6
5 Contours from numerical simulations at 61 km altitude 10
6 Contours from numerical simulations at 71 km altitude 10
6 Comparison of electron number density contours along the surface at 61 km and 71 km altitudes for NEQ models 11
7 Electron number density distribution along the capsule skin for varying wall temperatures 12
8 Electron number density distribution along the stagnation streamline for varying wall temperatures 13
9 Mass fraction distribution of atmospheric species along the stagnation streamline at an altitude of 61 km 13
9 Mass fraction distribution of atmospheric species along the stagnation streamline at an altitude of 61 km 14
10 Translational temperature distributions along the stagnation streamline at different altitudes for various models 15
11 Vibrational temperature distributions along the stagnation streamline at different altitudes for various models 15
12 Temperature distributions along the stagnation streamline at different altitudes for various multi-temperature models 16
13 Electron number density distributions at different altitudes for various multi-temperature models 17
14 Translational temperature distributions along the stagnation streamline at different altitudes for various multi-temperature and viscosity models 17
15 Vibrational temperature distributions along the stagnation streamline at different altitudes for various multi-temperature and viscosity models 18
16 Electronic temperature distributions along the stagnation streamline at different altitudes for various multi-temperature and viscosity models 18
17 Electron number density distributions at different altitudes for various multi-temperature models and viscosity models 19
18 Electron number density distributions at 61 km for various vibrational relaxation time and chemistry models at thermo-chemical non-equilibrium 20
19 Electron number density distributions at 61 km for various vibrational relaxation time and chemistry models at chemical non-equilibrium 20
20 Mass fraction distributions of atmospheric species along the stagnation streamline at an altitude of 71 km 23

List of Tables

1 Chemical species considered in each air model 7
2 Initial mass fractions at the inflow boundary 8
3 Conditions for RAM-C II test cases 9
4 Model configurations selected at each altitude for wall temperature sensitivity study 12

1 Introduction

The accurate prediction of hypersonic flow phenomena during atmospheric re-entry is crucial for the design and safe operation of spacecraft. One key challenge is modeling the complex thermo-chemical processes that govern the behavior of the shock layer formed around the vehicle, which affects parameters such as electron number density and leads to phenomena like radio-frequency blackout.

Hypersonic flows at Mach numbers on the order of 20, typical of re-entry trajectories, result in extreme aerodynamic heating and strong shock waves. These conditions cause the atmospheric gas to dissociate and partially ionize in the shock-compressed layer near the vehicle surface. The intensity of these physico-chemical processes varies significantly with altitude.

This report focuses on the Radio Attenuation Measurement C (RAM-C) flight experiments conducted by the National Aeronautics and Space Administration (NASA), which provide valuable data on plasma formation. The RAM-C dataset, including detailed trajectory and plasma measurements, serves as a benchmark for validating computational tools that simulate such non-equilibrium physico-chemical phenomena in hypersonic flows.

The numerical methodology employed here involves solving the Navier–Stokes equations coupled with detailed thermo-chemical non-equilibrium models. Various chemical kinetics and boundary condition models are tested to determine which best reproduce the RAM-C flight observations.

The objectives of this work include validating simulation results against RAM-C flight data, with a particular focus on predicting electron number density. Additionally, the study examines predicted mass fractions and temperatures along the stagnation streamline to compare the performance of different models, despite the absence of experimental data for these quantities.

The report presents a comprehensive comparison of predicted and measured quantities across different flight altitudes and discusses the implications for precise and reliable prediction of re-entry parameters.

2 RAM-C flight experiments

A series of experiments called Radio Attenuation Measurement for study of communications blackout (RAM-C) were performed in the United States in the last 60s. The main purpose of these experiments was to measure the electron density in the compressed layer of spacecraft entering the atmosphere at hypersonic velocity.

NASA's RAM-C I and II vehicles were flown in October 1967 and August 1968, respectively. Both vehicles featured a hemisphere–9° cone configuration with nose radius of $r = 15.24\,\text{cm}$.

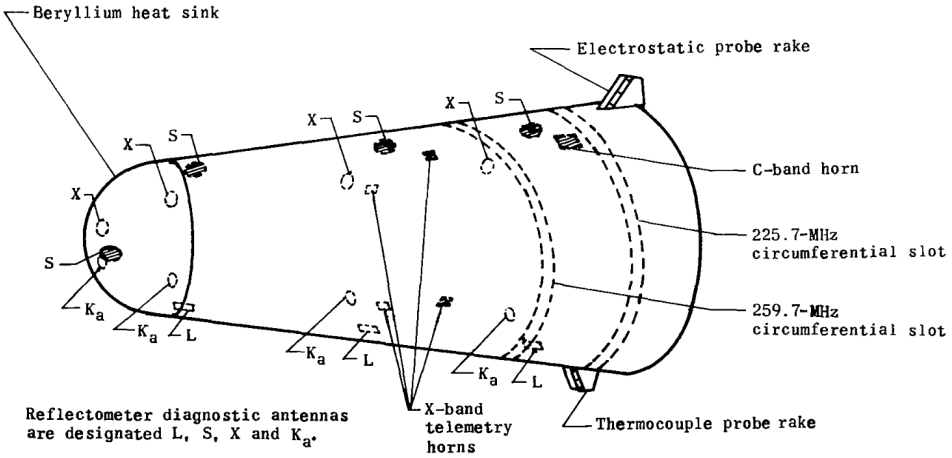

Figure 1: Schematic of RAM-C II with probe and antenna locations from [1]

A complete description of RAM-C I, including its instrumentation, data, and other details, is provided by Akey and Cross [2]. A similar account of RAM-C II is given by Grantham [3].

The experimental data of these flights are of particular value because a significant fraction of the indicated flight data corresponds to conditions of the absence of thermal equilibrium.

3 Simulation configuration

3.1 Geometry & meshing

The RAM-C vehicle was modeled using an axi-symmetric approximation, consistent with its geometry and the absence of angle of attack during the flight. This simplification reduces computational cost while preserving the essential physical features of the flow.

A structured mesh was used to discretize the flow domain. The mesh was designed to resolve the bow shock and the boundary layer with sufficient accuracy. Grid clustering was applied near the vehicle surface and in regions of strong gradients.

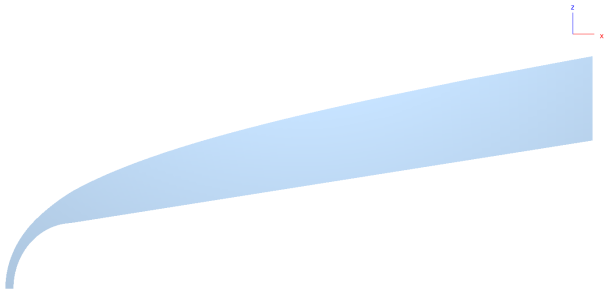

Figure 2: Modeling of the RAM-C geometry

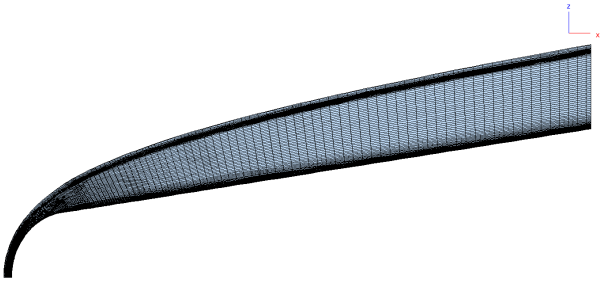

Figure 3: Overview of the mesh used

Figure 2 shows the 2D modeling of the RAM-C geometry, while Figure 3 provides an overview of the computational mesh used in the simulations.

3.2 The NSMB solver

All CFD computations in this study were performed using the Navier–Stokes Multi Block (NSMB) solver, developed by a consortium of universities and industry partners [5]. NSMB is a parallelized, cell-centered finite volume solver designed for compressible flows on structured multi-block grids.

The code supports both explicit and implicit time integration schemes, with second- and fourth-order central discretizations (with artificial dissipation), as well as several upwind schemes up to fifth order. Turbulence modeling includes validated RANS models (up to 5 equations), LES, hybrid RANS–LES, and transition models.

NSMB was originally developed with hypersonic applications in mind, such as atmospheric re-entry. It includes various levels of chemical modeling for air, CO_2, and N_2, with available air models incorporating 5, 7, 11, or 13 species. Non-equilibrium models include those by Park (1989–2001), Gardiner, and Dunn–Kang, using equilibrium constants computed from polynomial fits (further details available in [5]).

Thermo-chemical non-equilibrium is modeled via the Landau–Teller theory for translational – vibrational energy exchange, with Millikan–White relaxation times. Transport coefficients are computed using the Blottner model or the Gupta-Yos model. Both inviscid and viscous flows (laminar and turbulent) are supported. Wall boundary conditions allow for super- and partially catalytic surfaces.

Furthermore, to improve numerical stability in shock-dominated flows, NSMB includes a bow shock adaptation capability. This feature adjusts the far-field boundary to a position near the shock location, tracked via the Mach number. The grid lines are then adaptively redistributed around the shock location. The grid needs to be adapted generally two to three times to obtain a converged shock position.

NSMB has been employed extensively in various European projects, demonstrating its versatility and robustness across a range of aerodynamic applications.

3.3 Numerical parameters

The simulations were carried out using the following numerical parameters. A total of 15 000 time steps (`NSTEPS`) were performed to advance the solution toward convergence. The Courant–Friedrichs–Lewy (CFL) number was set to 0.5 to ensure numerical stability. An implicit time integration scheme was employed, allowing for larger time steps and improved stability in capturing the flow features of hypersonic regimes.

For spatial discretization, a central differencing scheme was used in combination with artificial dissipation. The standard dissipation model was adopted for this simulation.

To accurately capture shock waves and steep gradients, an `automatic` shock adaptation was performed in four successive stages. The adaptation process is triggered when the shock is sufficiently well-defined, meaning it exhibits a strong gradient across adjacent cells. After completing these adaptation stages, the simulation was continued for an additional 5 000 steps to reach the final steady-state solution. Figures 4a and 4b illustrate the outcome of the shock adaptation process. The first figure displays the resolved shock interface through the Mach number distribution, while the second shows the localized mesh refinement in the corresponding region.

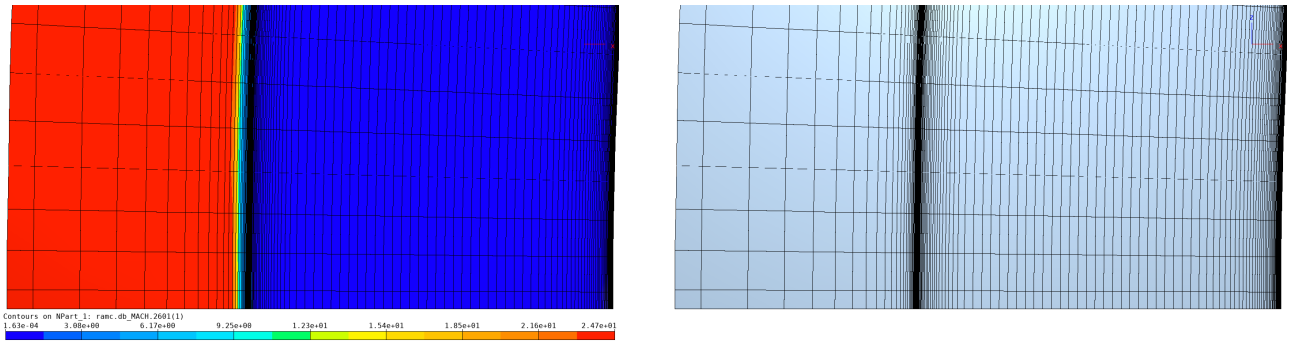

(a) Shock interface through Mach number

(b) Localized mesh refinement

Figure 4: Shock adaptation of the mesh

3.4 Flow model

The simulations were conducted under the assumption of steady-state conditions. A laminar flow model was employed, appropriate for the flow regime under consideration. Viscous effects were modeled using the Blottner viscosity model with the Eucken correction to account for the thermal conductivity effects.

3.5 Kinetic model

The assumption of a quiescent, chemically frozen atmosphere at inflow is applied. The following assumptions are made at the inflow boundary:

- The air is considered a reacting gas mixture, composed of multiple species, including both neutral and ionized components.
- The inflow temperature and pressure are such that only the major neutral species (N_2, O_2) are present in significant amounts, while minor species and ionized components are initialized at trace concentrations.
- A 7-species or 11-species air model is selected depending on the study carried out.

3.5.1 Chemical species

The chemical species considered are summarized in Table 1.

7-species air model	11-species air model
Molecular nitrogen (N_2)	Molecular nitrogen (N_2)
Molecular oxygen (O_2)	Molecular oxygen (O_2)
Nitric oxide (NO)	Nitric oxide (NO)
Atomic nitrogen (N)	Atomic nitrogen (N)
Atomic oxygen (O)	Atomic oxygen (O)
Electrons (e^-)	Ionized nitric oxide (NO^+)
Ionized species	Ionized molecular nitrogen (N_2^+)
	Ionized molecular oxygen (O_2^+)
	Atomic nitrogen ion (N^+)
	Atomic oxygen ion (O^+)
	Electron (e^-)

Table 1: Chemical species considered in each air model

3.5.2 Chemical reactions

The key reactions considered for the 7-species air model, including dissociation, recombination, ionization, and charge exchange processes, are taken from [6]:

$$N_2 + M \rightleftharpoons 2N + M \quad (1)$$
$$O_2 + M \rightleftharpoons 2O + M \quad (2)$$
$$NO + M \rightleftharpoons N + O + M \quad (3)$$
$$N_2 + O \rightleftharpoons NO + N \quad (4)$$
$$NO + O \rightleftharpoons O_2 + N \quad (5)$$
$$N + O \rightleftharpoons NO^+ + e^- \quad (6)$$

where M represents any species acting as a third body to conserve energy and momentum.

For the 11-species air model, the following reactions are considered (as reported in [9]):

$$N_2 + M \rightleftharpoons 2N + M \quad (7)$$
$$O_2 + M \rightleftharpoons 2O + M \quad (8)$$
$$NO + M \rightleftharpoons N + O + M \quad (9)$$
$$N_2 + O \rightleftharpoons NO + N \quad (10)$$
$$NO + O \rightleftharpoons O_2 + N \quad (11)$$
$$N + O \rightleftharpoons NO^+ + e^- \quad (12)$$
$$N + N \rightleftharpoons N_2^+ + e^- \quad (13)$$
$$O + O \rightleftharpoons O_2^+ + e^- \quad (14)$$
$$N + e^- \rightleftharpoons N^+ + 2e^- \quad (15)$$
$$O + e^- \rightleftharpoons O^+ + 2e^- \quad (16)$$
$$N_2 + O_2^+ \rightleftharpoons N_2^+ + O_2 \quad (17)$$
$$NO^+ + N \rightleftharpoons O^+ + N_2 \quad (18)$$
$$NO^+ + O \rightleftharpoons N^+ + O_2 \quad (19)$$
$$NO^+ + O_2 \rightleftharpoons NO + O_2^+ \quad (20)$$
$$NO^+ + N \rightleftharpoons N_2^+ + O \quad (21)$$
$$O_2^+ + N \rightleftharpoons N^+ + O_2 \quad (22)$$
$$O^+ + NO \rightleftharpoons NO^+ + O \quad (23)$$
$$NO^+ + O \rightleftharpoons O_2^+ + N \quad (24)$$
$$O^+ + N_2 \rightleftharpoons N_2^+ + O \quad (25)$$

3.5.3 Mass fractions

We assume the atmosphere's air has the composition presented in Table 2.

Species	Mass fraction
N_2	0.76536
O_2	0.23464
N	1×10^{-12}
NO	1×10^{-12}
O	1×10^{-12}
NO^+	1×10^{-12}
e^-	1×10^{-12}

Table 2: Initial mass fractions at the inflow boundary

3.6 Thermo-chemical models

The kinetic model employed in this study accounts for thermo-chemical non-equilibrium effects, typical of hypersonic flow environments. These effects arise at high speeds and altitudes when the characteristic flow time around a hypersonic vehicle is comparable to or shorter than the time required for molecular collisions to restore equilibrium.

The initial vibrational temperature of the gas is set to 298.15 K. To model the vibrational relaxation behavior of diatomic molecules, several empirical models were considered for the vibrational relaxation time:

- Millikan-White (`mw`) model
- Millikan-White with Parks correction for high temperatures (`mwp`)
- MW-Kim (`mwkim`)

Chemical non-equilibrium effects are captured using `gas model 4`, while thermo-chemical non-equilibrium, where both chemical kinetics and internal energy mode relaxation are treated in a coupled manner, is modeled using `gas model 5`.

3.7 Boundary conditions

The inflow boundary conditions correspond to the experimental data reported in [1], [2] and [3]. The wall temperature was initially fixed at $T_{\text{wall}} = 1\,000\,\text{K}$. The surface is considered non-catalytic. Additionally, thermal equilibrium between the vibrational and wall temperatures was assumed at the streamlined surface, i.e. $T_{\text{vib}} = T_{\text{wall}}$.

Several variations of these boundary conditions were explored as part of numerical experiments. These included both increasing and decreasing the wall temperature to $T_{\text{wall}} = 1\,500\,\text{K}$ and $T_{\text{wall}} = 800\,\text{K}$ respectively.

4 Numerical simulation results

As previously noted, the data from the RAM-C II flight experiment have been extensively used in the literature to validate various physicochemical models of hypersonic flow. Among these studies, [6], [7], [8] present a comparison of the electron concentration distributions along a streamlined blunt cone at all three altitudes $h = 61, 71, 81$ km for which detailed flight measurements are available in [1]. However, due to the limited description of the kinetic model employed in [6], it is not possible to reproduce those results with complete accuracy.

Although dataset corresponding to $h = 81$ km is available, it will not be considered in the present study due to the limitations of the Navier–Stokes equations at such high altitudes, where rarefaction effects become non-negligible and continuum assumptions begin to break down.

The same computational mesh was used throughout all the simulations presented here. Only the boundary conditions were varied between configurations to isolate the influence of surface properties and assumptions.

4.1 Conditions for RAM-C II test cases

Table 3 presents the initial data for the numerical modeling as described in [6]. All input files were initialized using these conditions.

	Configuration 1	**Configuration 2**
Altitude (km)	61	71
$\mathbf{M_\infty}$	23.9	25.9
Re	19 500	6 280
$\mathbf{T_\infty}$ **(K)**	254	216
$\mathbf{p_\infty}$ **(Pa)**	19.7	4.764

Table 3: Conditions for RAM-C II test cases

4.2 Electron number density distribution along the capsule skin

The distribution of electron number density, N_e, is analyzed both along the surface of the vehicle and specifically along the stagnation streamline (discussed in detail later in Section 4.3.2). These regions are of particular interest due to the intense heating and ionization that occur in the hypersonic regime.

Examples of the electron number density contours obtained at altitudes of 61 km and 71 km for a specific model configuration are presented in Figures 5 and 6. These results correspond to the simulation case using the 7-species air model under Park's 2001 thermo-chemical non-equilibrium model, with a fixed wall temperature of 1 000 K and a non-catalytic surface assumption.

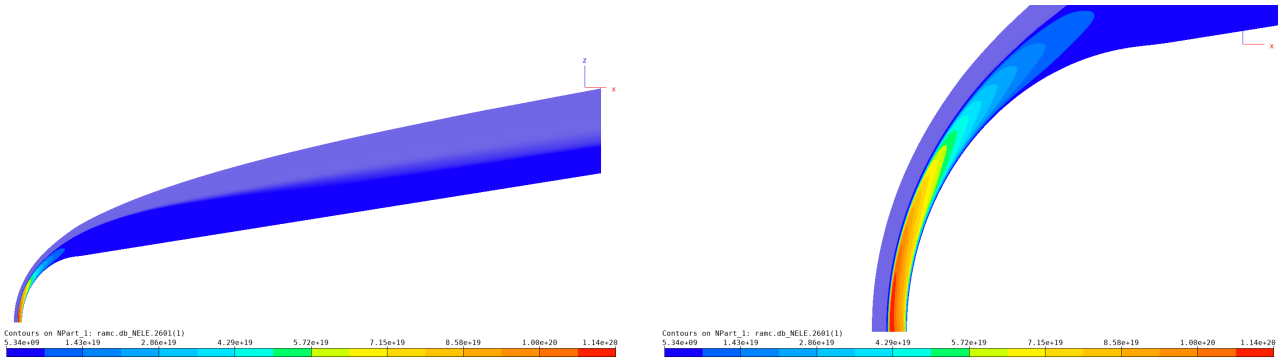

(a) Overall electron number density (b) Zoomed view of electron number density

Figure 5: Contours from numerical simulations at 61 km altitude

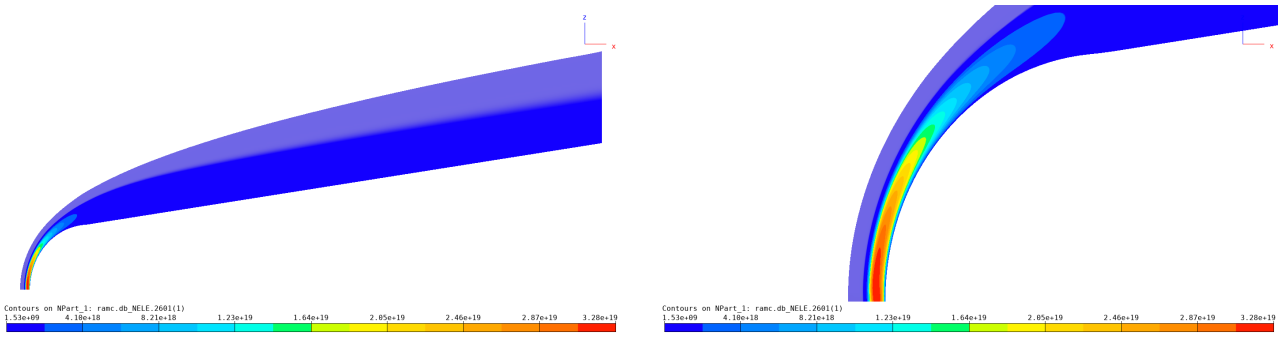

(a) Overall electron number density (b) Zoomed view of electron number density

Figure 6: Contours from numerical simulations at 71 km altitude

These figures provide a general overview of the plasma distribution in the flow field. The results are derived from the numerical simulations performed for this study. As seen in the figure, the maximum electron number density is observed near the stagnation point, directly ahead of the vehicle's nose where the shock is strongest and thermal ionization is greatest. The peak values reach approximately $1.14 \times 10^{20}\,\mathrm{m}^{-3}$ at 61 km and $3.28 \times 10^{19}\,\mathrm{m}^{-3}$ at 71 km.

At 61 km, the atmosphere is still dense enough to support significant ionization. The simulation shows a well-defined ionization layer forming in front of the nose, with high electron densities concentrated near the stagnation point and gradually decreasing along the body surface.

At 71 km, the atmospheric density decreases, leading to less collisionality and a thinner ionization layer. The peak electron number density remains localized around the stagnation region but is lower in magnitude compared to the 61 km case, reflecting the diminished intensity of shock-induced ionization.

A comparative overview of the computed electron number density results for the different modeling configurations is presented in Figure 6.

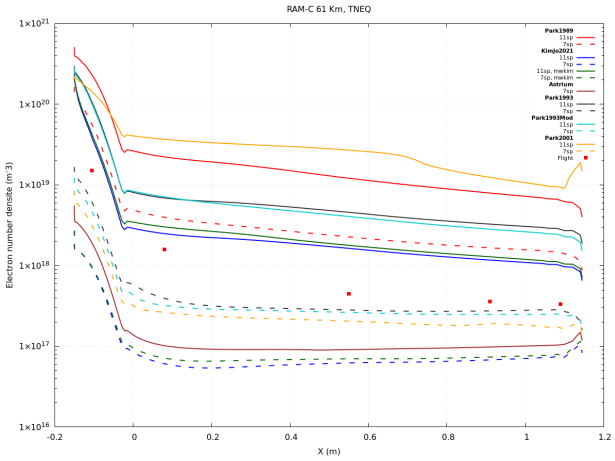

(a) TNEQ models at 61 km

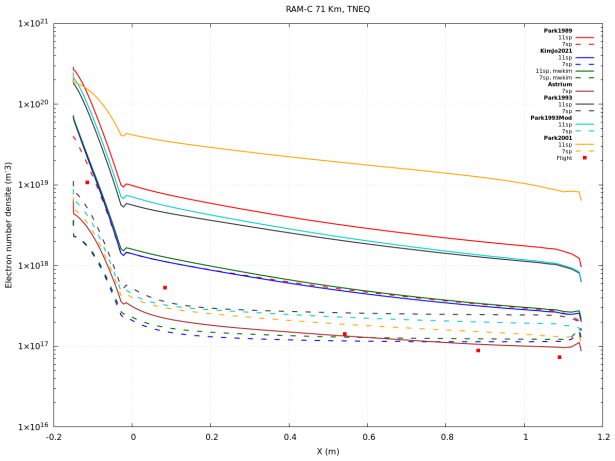

(b) TNEQ models at 71 km

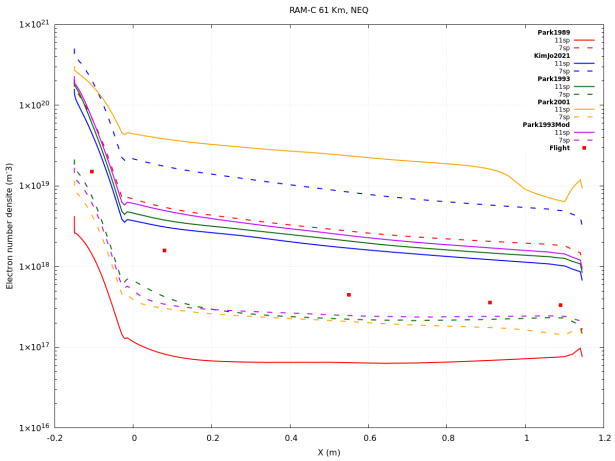

(c) NEQ models at 61 km

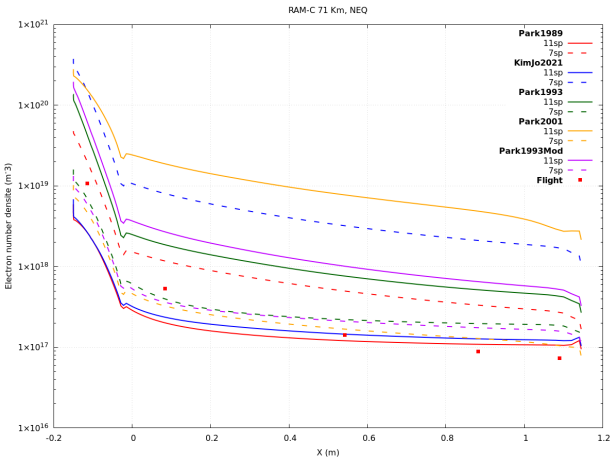

(d) NEQ models at 71 km

Figure 6: Comparison of electron number density contours along the surface at 61 km and 71 km altitudes for NEQ models

The curve behaviors appear generally consistent with similar trends along the capsule surface. For both altitudes, some models provide a closer match near the nose region, while others better capture the behavior along the skin. Furthermore, it seems easier to determine which model best fits the experimental data at an altitude of 61 km than at 71 km. The overestimations also tend to be more pronounced in configurations using the 11-species air model. Nonetheless, none of the models tested is able to reproduce the flight data with complete accuracy.

4.3 Wall temperature

Since the actual wall temperature for the test case is unknown, simulations were performed with wall temperatures varied as $T_{\text{wall}} = 800, 1\,500\,\text{K}$ to assess their impact on the accuracy of modeling the experimental dataset.

4.3.1 Distribution along the capsule skin

Models that appeared to best match the flight dataset in the previous computations were selected at each altitude and tested under varying wall temperature conditions. Table 4 lists these model configurations.

Model type	61 km	71 km
TNEQ	Park1993 (7 species) Park1993Mod (7 species)	KimJo2021 MWP (11 species) Park1993 MWP (7 species)
NEQ	Park1993 (7 species) Park1993Mod (7 species)	Park1993 (7 species) Park1993Mod (7 species)

Table 4: Model configurations selected at each altitude for wall temperature sensitivity study

Figure 7 provides the comparative curves of the electron number densities along the vehicle surface for the three wall temperatures considered.

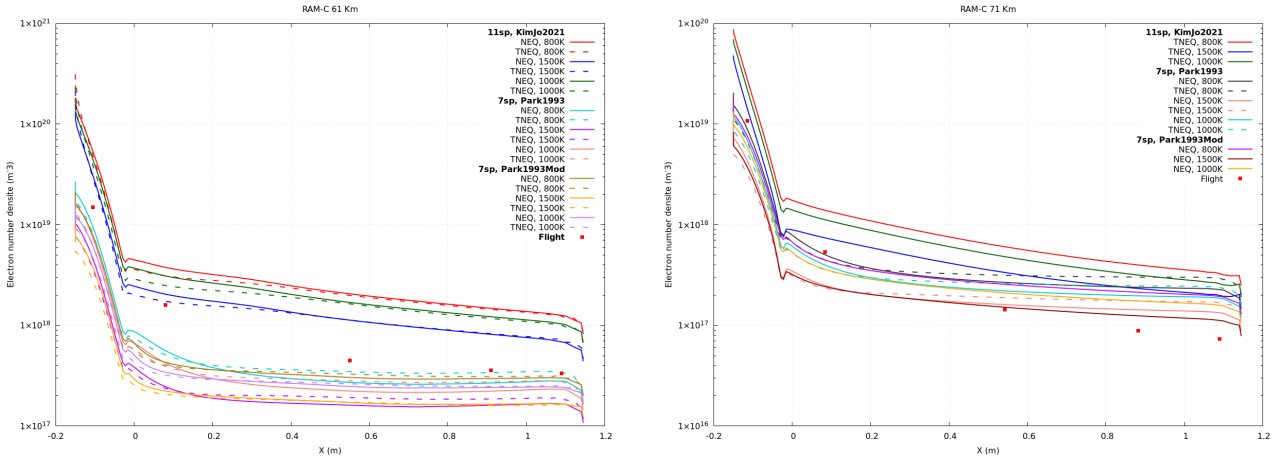

(a) At 61 km (b) At 71 km

Figure 7: Electron number density distribution along the capsule skin for varying wall temperatures

As shown in Figure 7, it remains difficult to clearly identify which model configuration and wall temperature provide the closest agreement with the flight dataset. Once again, certain models appear to better capture the behavior near the stagnation region, while others more accurately follow the trends along the capsule surface.

If a selection had to be made based on the current comparisons, the following models could be considered as the most representative of the experimental data for each altitude:

- At 61 km: TNEQ Park1993 7-species model at $T_{\text{wall}} = 800\,\text{K}$
- At 71 km: NEQ Park1993Mod 7-species model at $T_{\text{wall}} = 1500\,\text{K}$

In addition, the possible variation in wall temperature across altitudes seems consistent with physical, intuitive expectations, since the wall temperature is unlikely to remain uniform throughout the entire re-entry trajectory.

4.3.2 Distribution along the stagnation streamline

The electron number density was also examined along the stagnation streamline to visualize ionization effects in the region that presents the greatest gradient.

Since no experimental measurements are available along the stagnation line, this comparison serves primarily as a means to assess differences between models. The results presented in Figure 8 show that the general shape of the curves and the predicted electron concentrations are similar across configurations at a given altitude. This highlights consistent and stable trends.

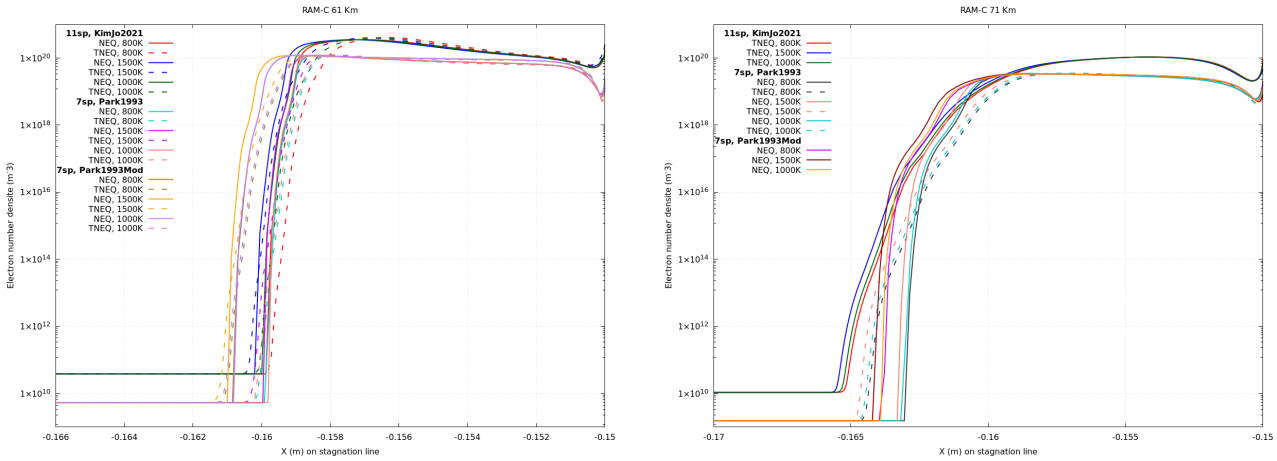

(a) At 61 km (b) At 71 km

Figure 8: Electron number density distribution along the stagnation streamline for varying wall temperatures

4.4 Mass fractions along the stagnation streamline

Although no experimental data is available, several studies in the literature, such as [6], have investigated mass fraction distributions along the stagnation streamline. Following this approach, mass fractions are also examined here along the stagnation line to further assess the influence of the different gas and air models as well as the wall temperature.

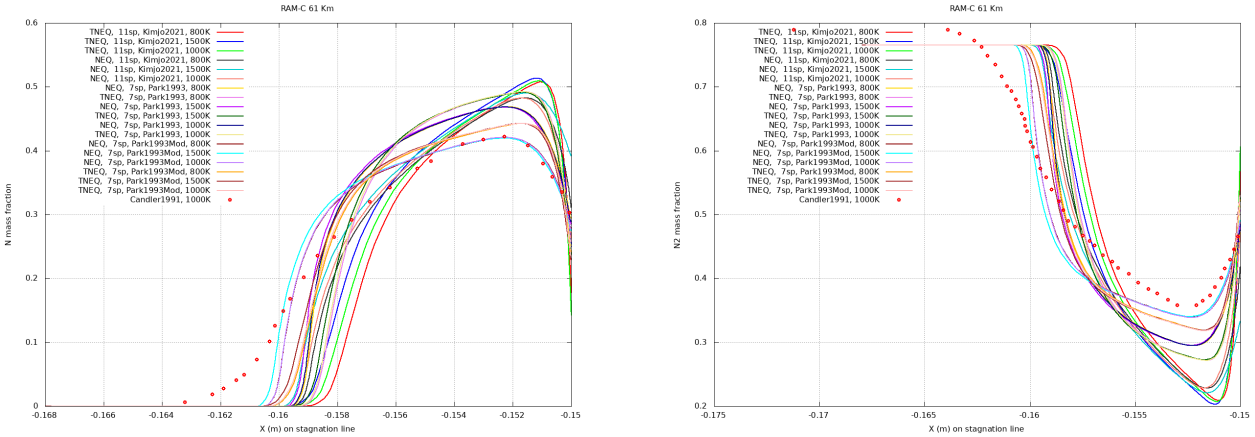

(a) N (b) N_2

Figure 9: Mass fraction distribution of atmospheric species along the stagnation streamline at an altitude of 61 km

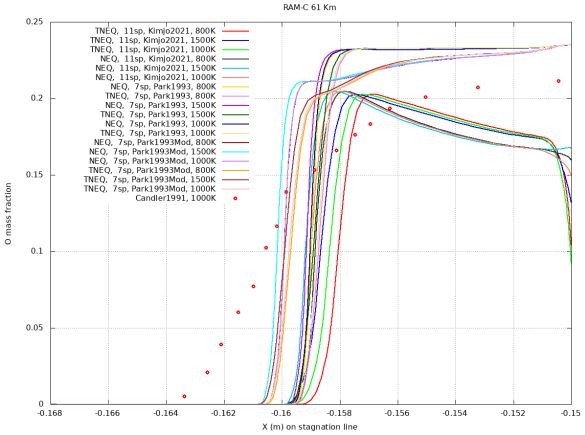

(c) O

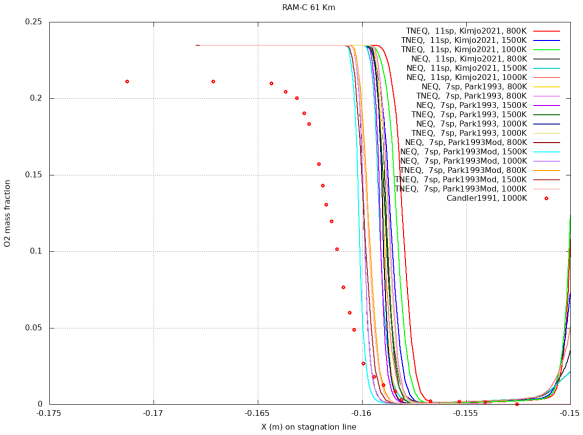

(d) O_2

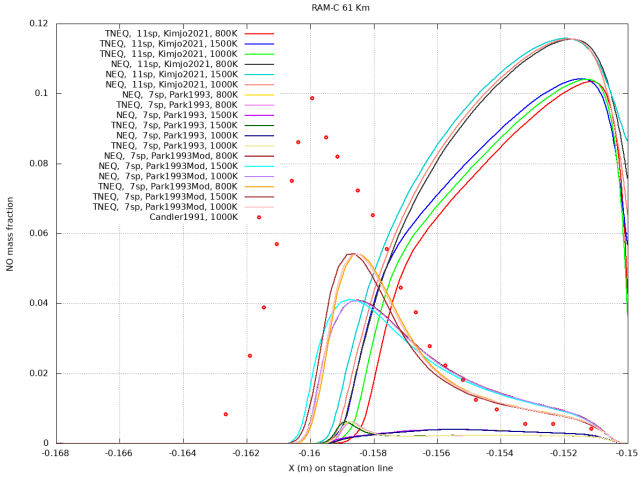

(e) NO

Figure 9: Mass fraction distribution of atmospheric species along the stagnation streamline at an altitude of 61 km

The overall shape of the plots is very similar across configurations. Furthermore, the numerical results remain very close, regardless of the number of species considered or the wall temperature used within a given model. Note that the study reported in [6] was made on a coarser grid without shock adaption, which explains that dissociation starts earlier.

However, Figure 9e does present noticeable discrepancies that remain unexplained.

The mass fraction distributions at an altitude of 71 km are provided in Appendix 20, where similar discrepancies for NO are observed.

4.5 Temperatures along the stagnation streamline

The distribution of thermodynamic temperatures along the stagnation streamline is key for accurately capturing the non-equilibrium effects that characterize hypersonic flows. In particular, differences between translational, vibrational, and electronic temperatures serve as an indicator of the degree of thermal non-equilibrium in the shock layer.

Figures 10 and 11 show the profiles of translational and vibrational temperatures respectively along the stagnation streamline at altitudes of 61 km and 71 km. The simulations were computed with a fixed wall temperature of $T_{\text{wall}} = 1\,000\,\text{K}$ and the Millikan–White model with Park's correction for the vibrational relaxation time.

The resulting temperature distributions are compared with reference results from the literature by Andrienko et al. [7], Esposito et al. [8], and Kim and Jo [9].

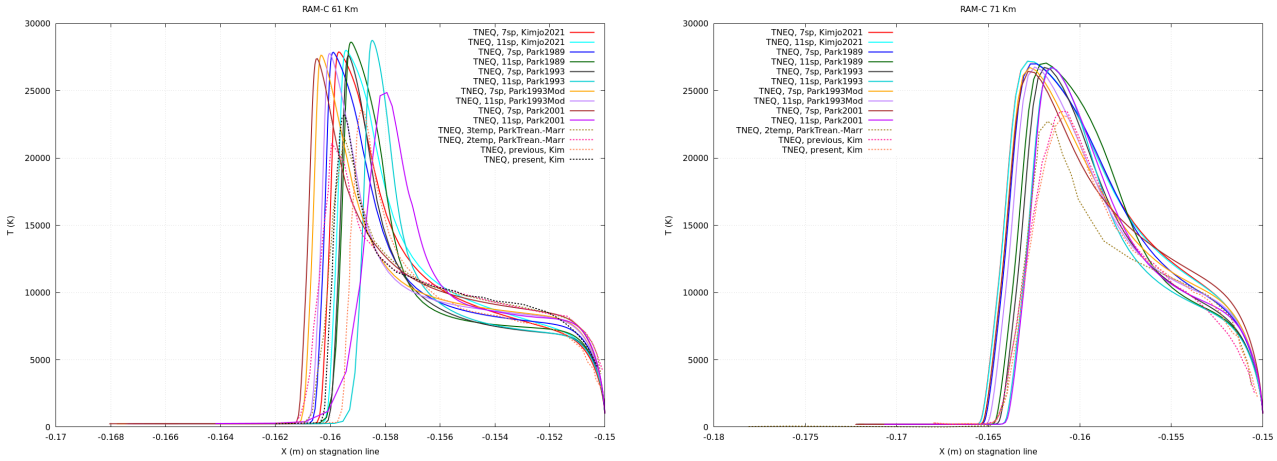

(a) At 61 km (b) At 71 km

Figure 10: Translational temperature distributions along the stagnation streamline at different altitudes for various models

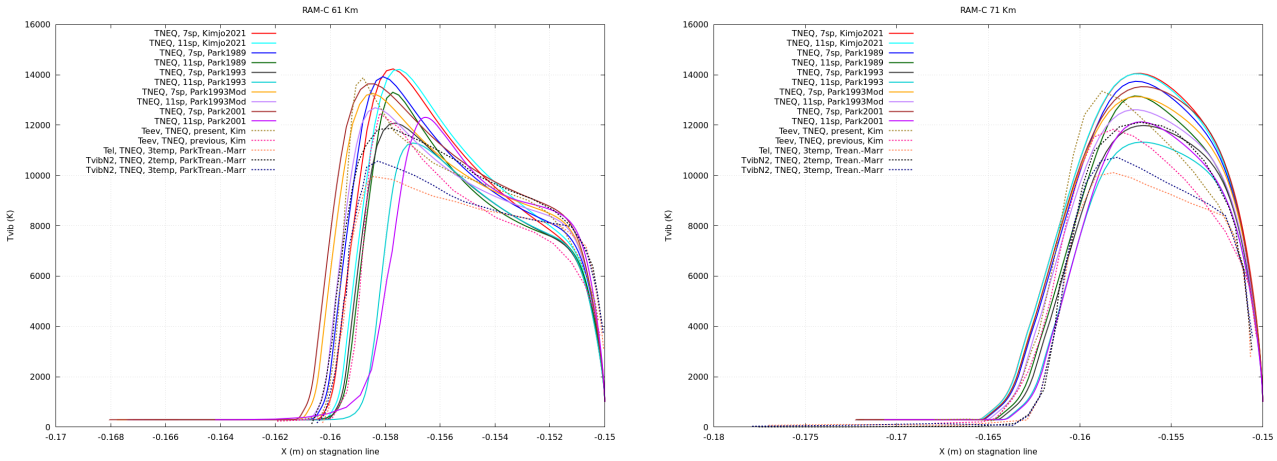

(a) At 61 km (b) At 71 km

Figure 11: Vibrational temperature distributions along the stagnation streamline at different altitudes for various models

The overall shape of the curves is very similar across all configurations, and the temperature variations remain within the same order of magnitude. Thus, the NSMB models seem largely in agreement with the literature although some slight overestimations can be noticed, particularly for the translational temperatures as seen in Figure 10. This slight overestimation might be due to a better capturing of the bow shock wave through the use of shock adaption.

4.6 Multi-temperature model sensitivity analysis

Until now, the two-temperature (2-T) model developed by Park was employed, which separates translational-rotational energy from the combined electron-electronic-vibrational energy, enabling thermo-chemical non-equilibrium modeling. Here, we adopt the three-temperature (3-T) model that extends the 2-T approach by further separating the energy of free electrons into a third temperature: electron-electronic temperature T_e. This provides improved accuracy in predicting electron behavior, especially given their distinct dynamics compared to heavier particles. While the 2-T model shows good agreement with experimental electron density, it lacks fidelity in representing free electron energy states. The 3-T model enhances this by treating electron energy separately, improving accuracy for flows with strong electronic non-equilibrium.

The results are primarily compared against the recent study by Kim [10], which provides detailed reference data for multi-temperature modeling. Thus, the wall temperature is fixed to $T_{\text{wall}} = 1\,200\,\text{K}$ and the surface is considered non-catalytic for a comparative framework. Initially, the air chemistry model uses Park's 1993 data, including recent modifications, and applies the Millikan–White formulation with Park's high-temperature correction for vibrational relaxation times.

Figures 12 to 19 illustrate the influence of multi-temperature models and transport property formulations on the flow behavior along the stagnation streamline and the capsule wall at altitudes of 61 km and 71 km.

4.6.1 Electronic non-equilibrium

The viscosity model remains unchanged in this section: the Blottner-Eucken model is still employed.

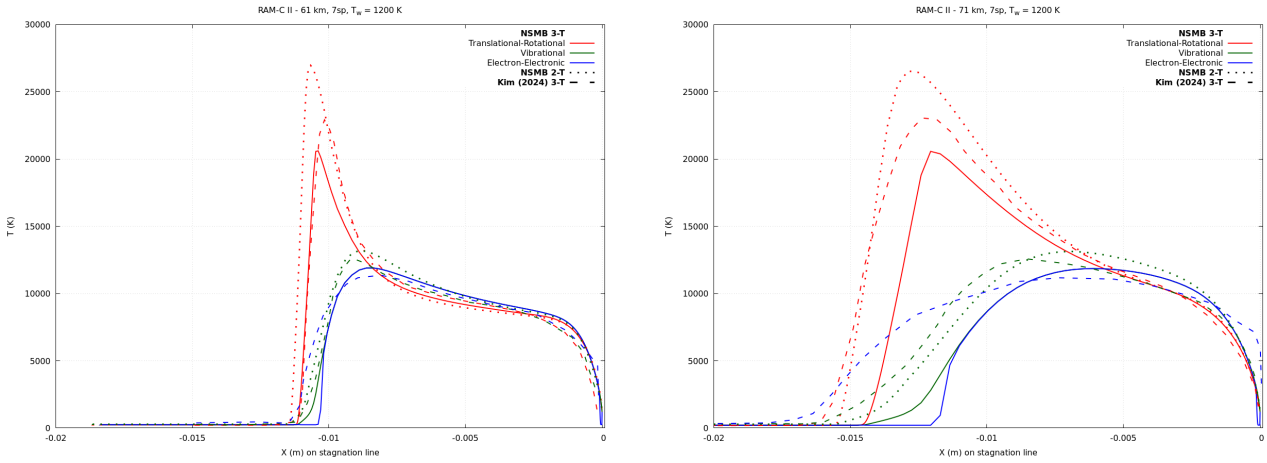

(a) At 61 km (b) At 71 km

Figure 12: Temperature distributions along the stagnation streamline at different altitudes for various multi-temperature models

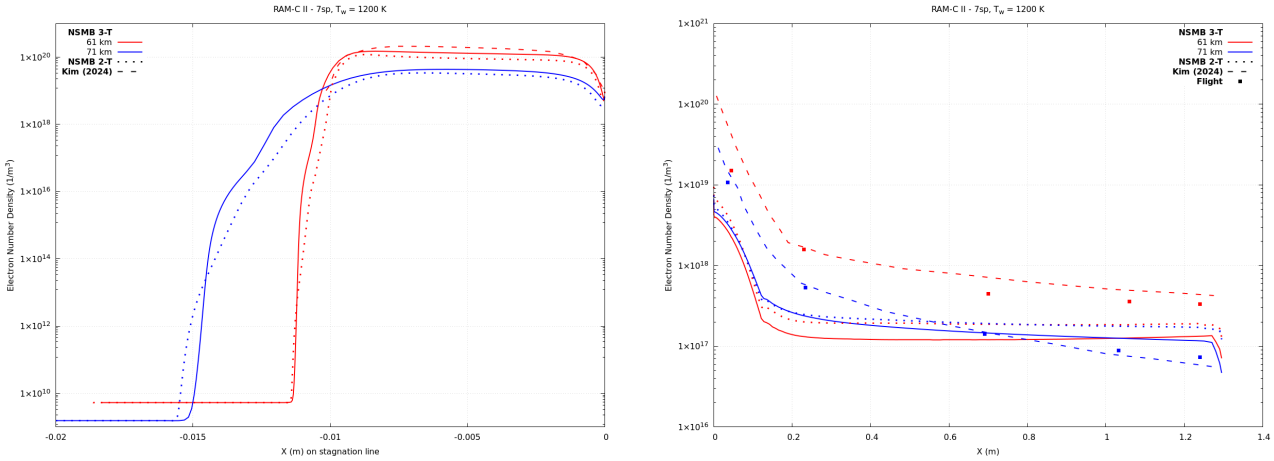

(a) On stagnation streamline (b) Along the wall

Figure 13: Electron number density distributions at different altitudes for various multi-temperature models

The comparison between the 2-T and 3-T models shows that the additional resolution of the electron-electronic energy leads to noticeable changes in the thermal field magnitudes, but has limited influence on their profiles. While both approaches yield similar vibrational temperatures, the 3-T model predicts both higher translational and electronic temperatures. This refinement is particularly evident at 71 km, where electronic non-equilibrium is stronger. The electron number density distributions (Fig. 13) confirm this trend: the 3-T model achieves closer agreement with the reference data of [10], highlighting the importance of explicitly accounting for the distinct electron dynamics.

4.6.2 Viscosity model influence

A sensitivity study on the viscosity model is conducted by comparing the Blottner–Eucken and Gupta–Yos formulations.

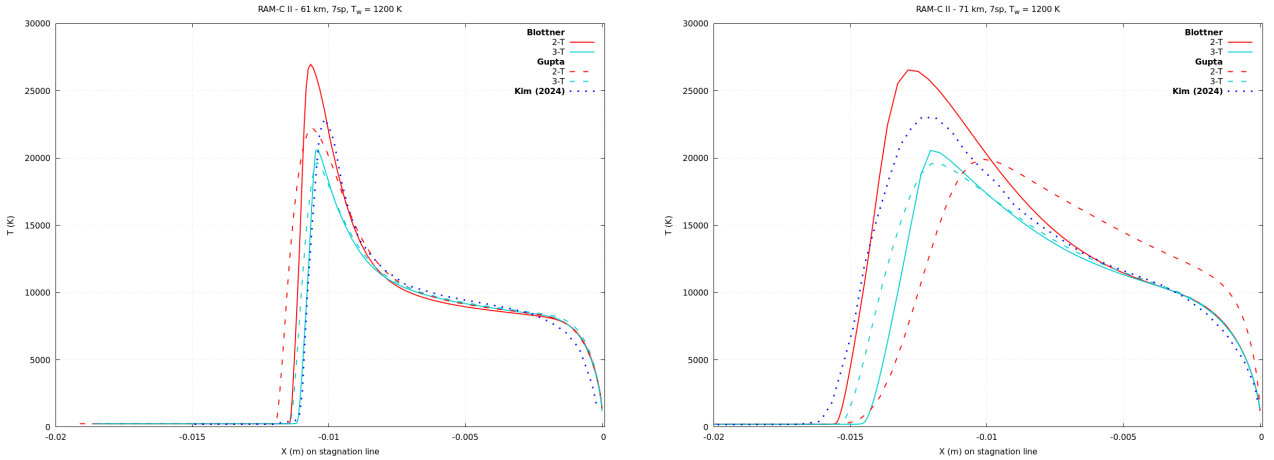

(a) At 61 km (b) At 71 km

Figure 14: Translational temperature distributions along the stagnation streamline at different altitudes for various multi-temperature and viscosity models

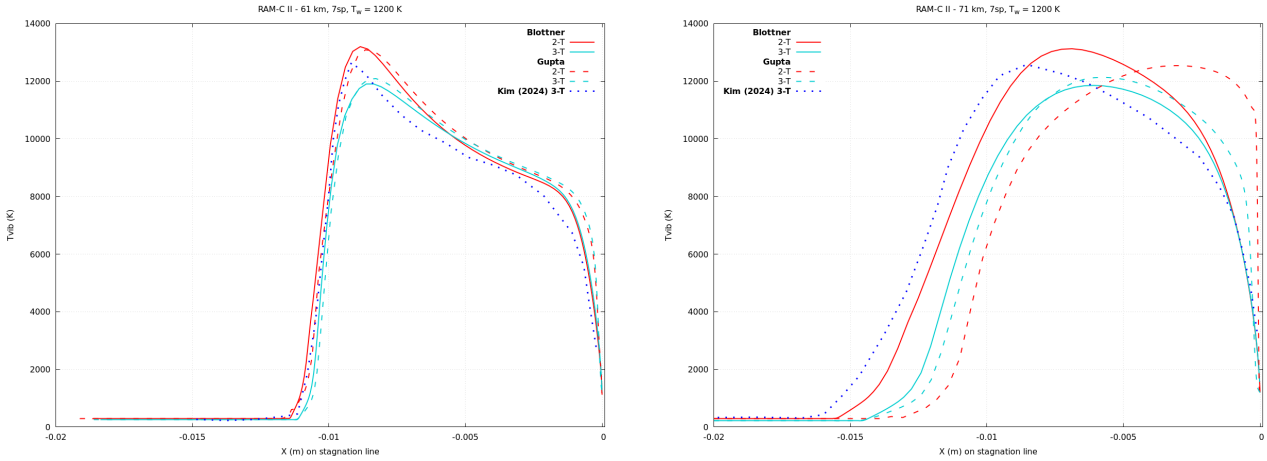

(a) At 61 km (b) At 71 km

Figure 15: Vibrational temperature distributions along the stagnation streamline at different altitudes for various multi-temperature and viscosity models

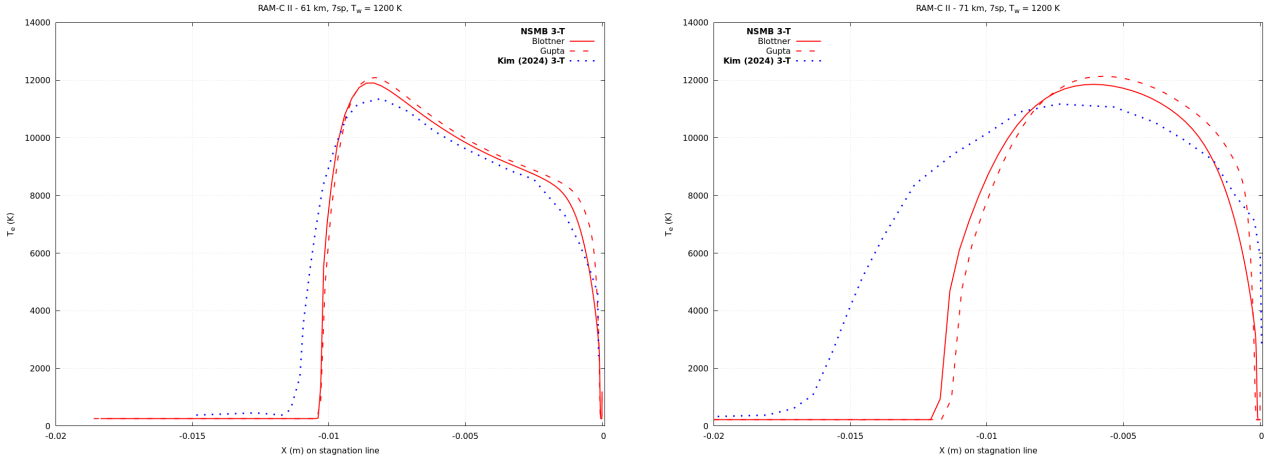

(a) At 61 km (b) At 71 km

Figure 16: Electronic temperature distributions along the stagnation streamline at different altitudes for various multi-temperature and viscosity models

Switching from the Blottner–Eucken to the Gupta–Yos viscosity model modifies the translational temperature distribution (Fig. 14). The lower effective viscosity in the Gupta–Yos formulation reduces shock heating, resulting in lower translational temperatures and, consequently, reduced ionization rates. This manifests as a global decrease in electron number density along the wall (Fig. 17) compared to the Blottner-based simulations. The vibrational and electronic temperature profiles (Figs. 15 and 16) show less influence from this change with only a slight shift in magnitudes.

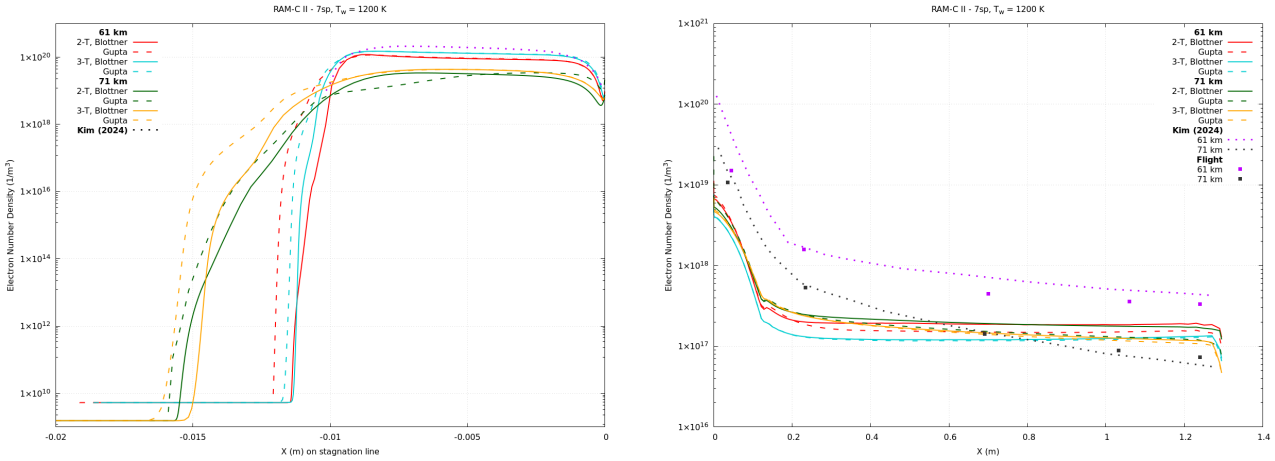

(a) On stagnation streamline (b) Along the wall

Figure 17: Electron number density distributions at different altitudes for various multi-temperature models and viscosity models

Overall, the simulations reproduce the main trends observed by Kim [10], notably the sensitivity of electron density predictions to both the choice of thermo-chemical model and the transport properties. However, the levels of electron density still show some deviations, particularly along the wall. Experimental data has not been precisely replicated.

4.6.3 Influence of non-equilibrium chemistry and vibrational relaxation time

In non-equilibrium gas dynamics, the vibrational relaxation time governs the rate at which molecular vibrational energy equilibrates following disturbances such as shocks. This is particularly critical in high-speed and high-altitude flows, where energy modes (translational, rotational, vibrational, electronic) may relax on different timescales.

These relaxation times are commonly estimated using the Millikan–White correlation, which, despite its widespread use, has two main limitations: its $T^{-1/3}$ temperature dependence often underestimates relaxation times at high temperatures (necessitating corrections such as Park's [12]) and its reliance on limited experimental data, restricting its generalizability. For example, Millikan and White primarily considered relaxation times for N_2–N_2, O_2–O_2, and O_2–Ar collisions, omitting many relevant interactions in air mixtures involving N, O, and NO. As a result, full air mixtures (including Ar) require computation of up to 18 distinct relaxation times, many of which fall outside the scope of the original data set. [11]

A sensitivity study on the vibrational relaxation time model is carried out by comparing results using the original Millikan-White correlation, Millikan–White with Park's high-temperature correction and Millikan–White with Kim's correction for both chemical non-equilibrium (Figure 19) and thermo-chemical non-equilibrium (Figure 18).

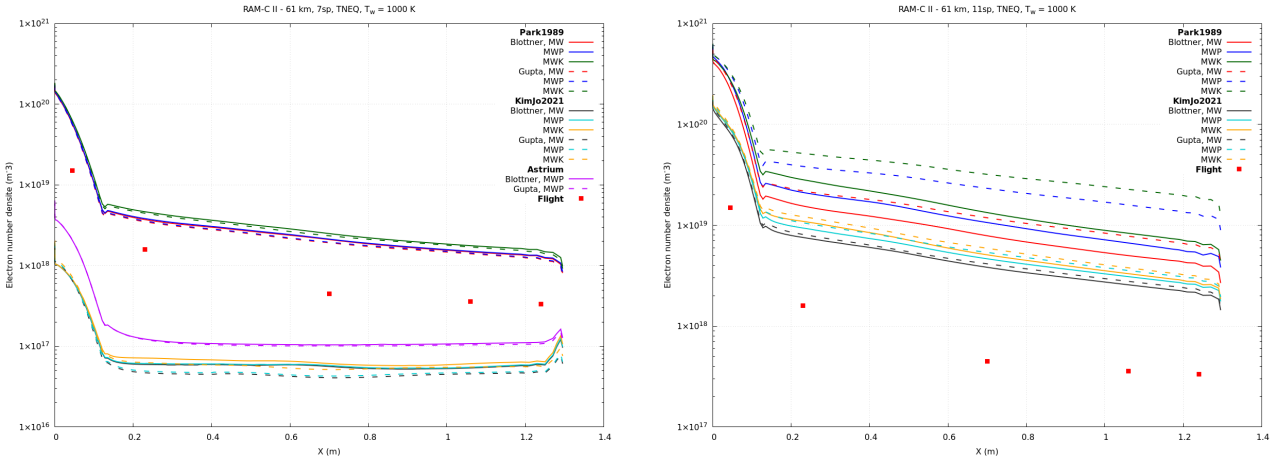

(a) 7 species (b) 11 species

Figure 18: Electron number density distributions at 61 km for various vibrational relaxation time and chemistry models at thermo-chemical non-equilibrium

For the 7-species model under thermo-chemical non-equilibrium, the chemistry model appears to have the strongest influence, regardless of the vibrational relaxation time or viscosity models. Park's 1989 chemistry model predicts significantly higher electron number densities at the stagnation point with up to two orders of magnitude greater than those from Kim & Jo (2021) and the Astrium model. No configuration matches the flight data and only minor differences are observed between vibrational relaxation time models within a given chemistry model.

The 11-species model consistently overpredicts the electron number density under thermo-chemical non-equilibrium. More pronounced differences are observed when varying the vibrational relaxation time model, particularly with Park's 1989 chemistry model.

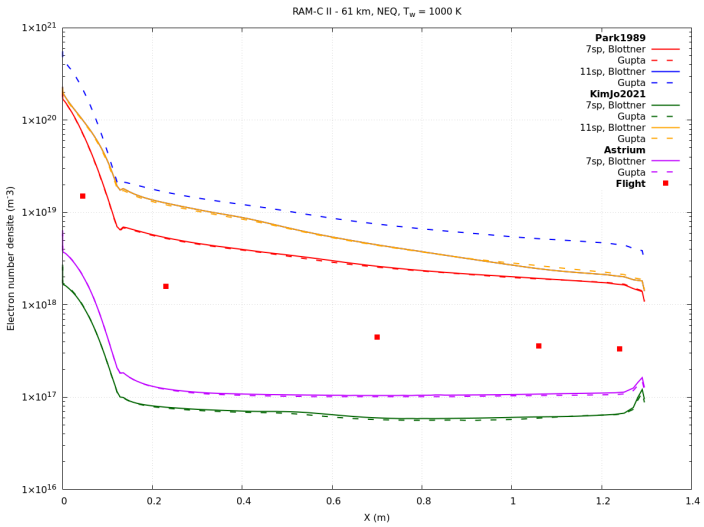

Figure 19: Electron number density distributions at 61 km for various vibrational relaxation time and chemistry models at chemical non-equilibrium

In chemical non-equilibrium, the behavior varies by chemistry model: Kim & Jo (2021) and Astrium's 7-species models underpredict electron densities, while other configurations tend to overpredict.

Electronic non-equilibrium simulations using the Astrium model for the 7-species case yield results that are nearly identical to its thermo-chemical non-equilibrium counterpart so was not added for clarity purposes.

Overall, none of the configurations achieve perfect agreement with experimental data. This raises questions about the probe positioning on the RAM-C vehicle, as discrepancies may arise if simulation data is not extracted from the same physical location as the flight measurement probe.

5 Conclusions

The CFD simulation results show satisfactory agreement with the RAM-C II flight experiment data across the studied altitude range. Various thermo-chemical models and boundary conditions were tested to identify the models that best reproduce the observed electron number densities measured during flight. The cross-comparison between the calculated and experimental electron number density distributions reveals a general underprediction by the 7-species model and an overprediction by the 11-species model. This trend has also been reported in the literature. However, ionization exchange reactions are largely neglected in the 7-species models but are accounted for in the 11-species models. While good agreement was achieved, many variables remain unknown and an accurate replication of the data was not possible.

Mass fractions and temperature profiles along the stagnation streamline were also examined, showing consistent trends despite the lack of direct experimental validation for these quantities.

Ultimately, while the current modeling approach effectively approximates the RAM-C flight data, the development of truly predictive and applicable thermo-chemical non-equilibrium models remains an active challenge for research in hypersonic flows.

References

[1] Jones, W.L. and Cross, A.E., *Electrostatic-probe measurements of plasma parameters for two re-entry flight experiments at 25,000 feet per second*, NASA, Langley Research Center, February 1972

[2] Akey, N.D. and Cross, A.E., *Radio blackout alleviation and plasma diagnostic results from a 25,000 foot per second blunt body re-entry*, NASA, 1970

[3] Grantham, W.L., *Flight results of 25,000 foot per second blunt body re-entry experiment using microwave reflectometers to measure plasma electron density and standoff distance*, NASA TN D-6062, 1970

[4] Surzhikov, S.T., *Numerical simulation of air ionization in the RAM-C-II flight experiment*, Fluid Dyn., 57 (Suppl. 2), S279–S298, 2022. DOI : 10.1134/S0015462822100639

[5] Hoarau, Y., Pena, D., Vos, J.B., Charbonnier, D., Gehri, A., Braza, M., Deloze, T., and Laurendeau, E., *Recent developments of the Navier-Stokes Multi Block (NSMB) CFD solver*, submitted to AIAA SciTech 2016, 4–8 Jan, San Diego, CA. DOI: 10.2514/6.2016-2056

[6] G. V. Candler and R. W. MacCormack, *Computation of Weakly Ionized Hypersonic Flows in Thermo-chemical Nonequilibrium*,AIAA Journal, 1993. DOI: 10.2514/3.260

[7] D. A. Andrienko, J. S. Shang, S. T. Surzhikov, and G. P. Huang, *Non-equilibrium Flow Field of RAM-C II Probe*, 45th AIAA Plasmadynamics and Lasers Conference, AIAA Aviation, 16–20 June 2014, Atlanta, GA. AIAA Paper 2014-2376. DOI: 10.2514/6.2014-2376

[8] S. Esposito and D. D'Ambrosio, *A Study on Plasma Formation on Hypersonic Vehicles Using Computational Fluid Dynamics*, Aerospace Europe Conference 2023 – 10th EUCASS – 9th CEAS, Politecnico di Torino, Torino, Italy. DOI: 10.13009/EUCASS2023-492

[9] J. G. Kim and S. M. Jo, *Modification of chemical-kinetic parameters for 11-air species in re-entry flows*, International Journal of Heat and Mass Transfer, vol. 173, 2021, Article 121221. DOI: 10.1016/j.ijheatmasstransfer.2021.121221

[10] Kim C., Kim K. H., Yang Y., Kim J. G., *Effect of multi-temperature models on heat transfer and electron behavior in hypersonic flows*, *Physics of Fluids*, Vol. 36, 096127, 2024. DOI: 10.1063/5.0223900

[11] Oblapenko G., *Calculation of Vibrational Relaxation Times Using a Kinetic Theory Approach*, *The Journal of Physical Chemistry A*, Vol. 122, 9844–9856, 2018. DOI: 10.1021/acs.jpca.8b09897

[12] Park C., *Review of Chemical-Kinetic Problems of Future NASA Missions, I: Earth Entries*, *Journal of Thermophysics and Heat Transfer*, Vol. 7, No. 3, pp. 385–398, 1993. DOI: 10.2514/3.431

Mass fraction distributions of atmospheric species along the stagnation streamline at an altitude of 71 km

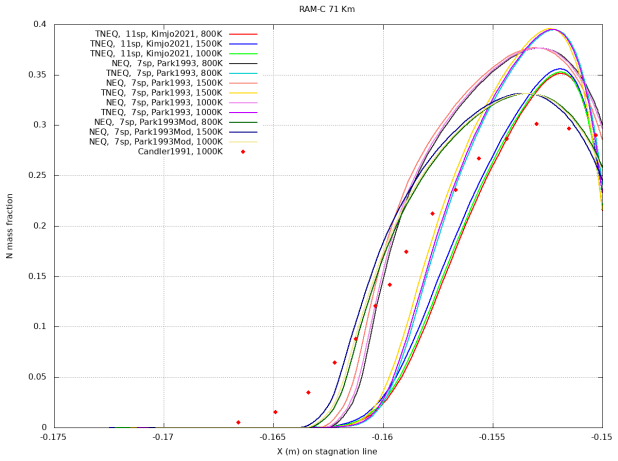

(a) N

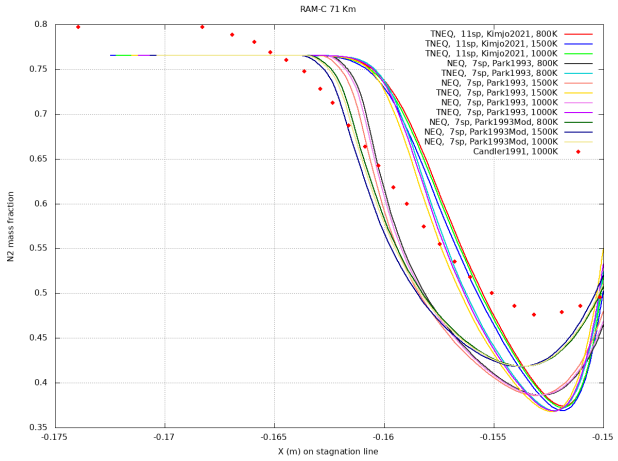

(b) N_2

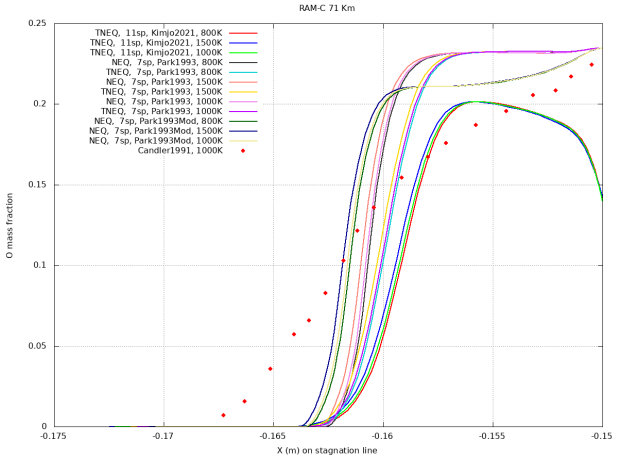

(c) O

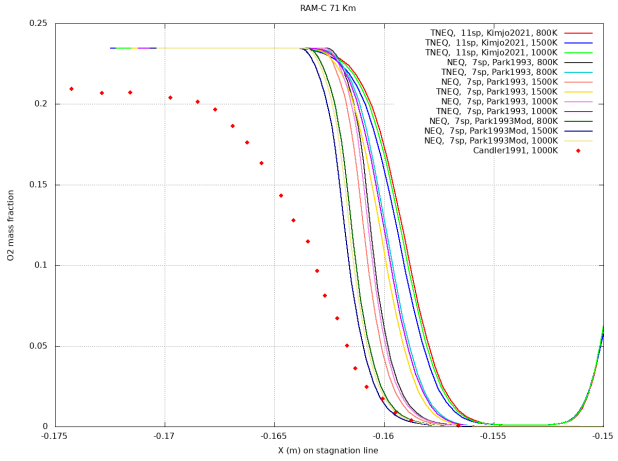

(d) O_2

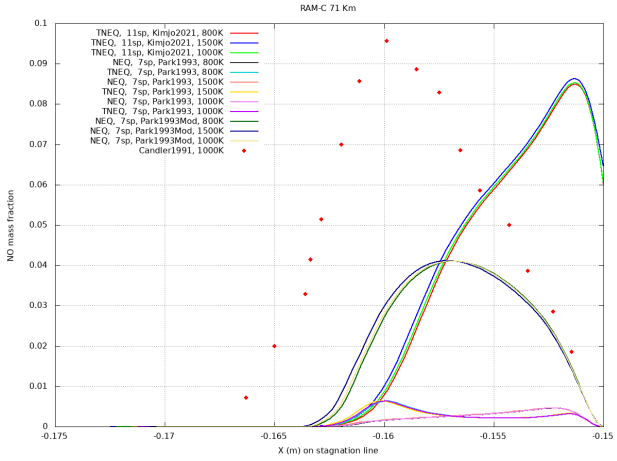

(e) NO

Figure 20: Mass fraction distributions of atmospheric species along the stagnation streamline at an altitude of 71 km